



The Role of Co-injected Helium on Swelling and Cavity Evolution at High Damage Levels in Ferritic-Martensitic Steels

D. Woodley^{a,*}, S. Taller^a, Z. Jiao^a, K. Sun^b, G.S. Was^{a,b}

^a Department of Nuclear Engineering and Radiological Sciences, University of Michigan, Ann Arbor, MI, 48109

^b Department of Materials Science and Engineering, University of Michigan, Ann Arbor, MI, 48109

ARTICLE INFO

Article history:

Received 4 November 2020

Revised 1 February 2021

Accepted 20 February 2021

Available online 28 February 2021

ABSTRACT

The influence of helium co-injection at rates from 0 to 4 appm He/dpa on swelling in ferritic-martensitic alloys T91 and HT9 was explored. Irradiations with 5.0 MeV Fe⁺⁺ ions and degraded He⁺⁺ ions were performed at 445°C up to damage levels of 150 dpa and helium co-injection rates of 0, 0.02, 0.2 and 4 appm He/dpa in T91, and at 460°C to a damage level of 188 dpa and helium co-injection rates of 0, 0.06 and 4 appm He/dpa in HT9. Helium was observed to enhance cavity nucleation at low damage levels, resulting in the maximum swelling at the highest helium co-injection rate. As the damage level was increased, the helium content at which swelling was maximized shifted to lower helium concentrations, ultimately resulting in the highest swelling occurring with zero helium by 150 dpa. This behavior was due to the helium-stabilized bubble microstructure that increased the cavity sink strength and reduced both cavity growth rate and swelling relative to the helium-free condition.

© 2021 Elsevier B.V. All rights reserved.

1. Introduction

Generation 4 reactors require relatively high damage levels and temperatures as compared to the current generation of reactors [1,2]. Ion irradiation is gaining interest as a surrogate for neutron irradiation because it is fast, cheap and effective [3–5]. However, ion irradiation does not include effects of transmutation that produces gasses such as helium, necessitating pre-implantation or co-injection. Helium has been shown to enhance cavity nucleation across many alloys systems [6,7,8,9,10,11,12,13]. However, studies on the influence of helium on the growth of cavities at high damage levels in ferritic-martensitic steels are limited. Smidt et al. [14] examined the behavior of EM-12 and HT9, two ferritic-martensitic steels, using heavy ions. Before irradiation, a 30 MeV helium beam was energy degraded using an aluminum sheet to obtain a half-Gaussian helium profile with an 11.8 micron full width half maximum with a peak concentration of 1 appm He. Irradiations with 2.8 MeV Fe⁺⁺ ions were performed up to 250 dpa at temperatures in the range 450–650°C to determine the temperature dependence of swelling. The authors did not consider the effect of helium concentration on swelling or the interplay between helium and temperature.

Kai and Kulsinki [15] implanted either 0 or 100 appm He into HT9 specimens and subsequently irradiated them up to 200 dpa. Cavities were only observed in the samples pre-implanted with 100 appm He, suggesting that helium was necessary to nucleate cavities. Since only one damage level was examined, no conclusions could be made about the effect of helium on growth.

Conversely, Toloczko et al. [16] conducted ion irradiation of ferritic ODS MA957, HT9 and EP-450 up to 500 dpa without implanted helium. In these experiments, a swelling rate of 0.2%/dpa was observed for both HT9 and EP-450 with total swelling exceeding 30% by 500 dpa for HT9, suggesting that helium was not required to facilitate the nucleation of cavities.

A more comprehensive examination of the effect of helium was been performed by Getto et al. [17]. The effect of pre-implanted helium was studied in HT9 with concentrations of 0, 1, 10 and 100 appm He. A difference in swelling rate was observed between 0, 10 and 100 appm He at 440°C and 480°C and between the 1 and 10 appm He conditions at 460°C. In general, higher amounts of helium resulted in a higher swelling rate, which was on the order of 0.02–0.04%/dpa [18]. Monterrosa et al. [12] covered a wider range of helium and damage levels. T91 was pre-implanted with 0, 1, 10, 100 and 1000 appm He and subsequently irradiated to damage levels up to 356 dpa at 460°C. A difference in swelling rate was observed between all helium levels with the maximum swelling rate observed for the lowest helium levels. This had the effect of shifting the maximum swelling from the sample with

* Corresponding author.

E-mail address: dawoodle@umich.edu (D. Woodley).

Table 1

Chemical composition (wt%) of alloy T91, heat 30176, provided by PNNL and Luvak, Inc., reproduced from [21] and alloy HT9, heat 84425 [23,24].

	C	N	Al	Si	P	S	Ti	V	Cr	Mn	Ni	Cu	Nb	Mo	W	Fe
T91 30176 (PNNL)	.08	.054	-	.11	-	-	-	.21	8.6	.37	.09	-	.072	.89	-	Bal.
T91 30176 (Luvak)	.091	.052	.004	.25	.007	.002	.003	.23	8.76	.44	.10	.062	.086	.86	.004	Bal.
HT9 84425	.21	.006	-	0.21	-	-	-	.33	11.8	.50	.51	-	-	1.03	.24	Bal.

10 appm He at 45 dpa to the sample without any helium at 356 dpa.

The previous studies were all performed with pre-implanted helium. Yamamoto et al. [19] irradiated F82H with helium co-injection rates of 15 to 55 appm He/dpa at a temperature of 500°C to damage levels of 10 and 26 dpa. At both damage levels, the maximum swelling was observed at 40 appm He/dpa. Similar behavior of a maximum swelling at the highest helium co-injection rate was found in T91 irradiated to 17 dpa and co-injected helium from 0 to 4 appm He [13]. However, the damage level is too low to draw any meaningful conclusions about the effect of helium on cavity growth and subsequent swelling.

While these studies demonstrate that the addition of helium enhances nucleation and increases cavity densities, particularly in pre-implanted samples, the effect of helium on cavity growth rate and swelling at high damage levels with co-injected helium remains unclear. Across these studies, multiple helium levels have been examined, all with variable behavior in swelling. The only systematic studies with co-injected helium were at a relatively low damage level [13,19]. Additionally, variations in alloy, irradiation temperature, damage level and helium implantation method further complicate the interpretation of the effect of helium. This work seeks to provide a clear understanding on the effect of co-injected helium to high damage levels on swelling by performing a comprehensive study on two alloys at a single temperature over three orders of magnitude helium injection rate.

2. Experiment

2.1. Sample preparation

Two ferritic-martensitic steels were used for this study. Alloy T91, heat 30176, was given a heat treatment consisting of normalization at 1038°C for 30 min followed by an air cool, and then tempering at 760°C for 30 min, again followed by an air cool [20]. This alloy has been previously irradiated and characterized for swelling and other microstructural features in both reactor [21] and dual ion irradiation (5 MeV Fe⁺⁺ with energy-degraded He⁺⁺) [13,22]. Alloy HT9, heat 84425, was given a heat treatment consisting of a 30 min normalization at 1065°C followed by an air cool, and then tempering at 750°C for 60 min, again followed by an air cool [23,24]. Samples were cut from an archive fuel duct and the same heat was used in the ACO-3 duct in the Fast Flux Test Facility (FFTF) [20,25]. A comparison of the composition in weight percent is shown in Table 1 as provided by both PNNL and Luvak for alloy T91.

Samples were cut in the form of 1.5 mm × 1.5 mm × 20 mm bars using electrical discharge machining, and then subsequently cut in half using a low speed diamond saw for final dimensions of 1.5 mm × 1.5 mm × 10 mm. The bars were then mechanically polished with silicon carbide paper using grits of 400, 600, 800 and 1200. The surface was then polished to a mirror finish using diamond slurries from 3 μm to 0.25 μm. After the mechanical polishing, the samples were electropolished for 20 s in a 90% methanol and 10% perchloric acid solution at temperatures between -40 and -50°C with an applied voltage of 40 V between the specimen and the platinum mesh.

2.2. Ion irradiations

The specimens were irradiated using the dual-beam configuration at the Michigan Ion Beam Laboratory (MIBL) at the University of Michigan [26]. A 5.0 MeV defocused Fe⁺⁺ beam from a 3 MV NEC Pelletron accelerator impinged normal to the sample surface and produced a damage rate of $7-9 \times 10^{-4}$ dpa/s. Simultaneously with the Fe⁺⁺ ion beam, helium from a 1.7 General Ionex Tandem accelerator with energy ranging from 2 to 2.85 MeV, depending on the thickness of the aluminum foil energy degrader, and raster-scanned at an angle of 60° to the sample normal to simulate transmutation gases. The degrader produced He ion energies between 0.2 and 1.2 MeV and were distributed so as to produce a fixed appm He/dpa over the depth range 300 to 1000 nm. Since the samples were polycrystalline and the lath sizes were small enough to catch multiple laths within both the length and depth of a liftout, sample orientation relative to the beam was not measured.

The damage level for each irradiation was calculated at a depth of 600 nm from the sample surface using SRIM in quick Kinchin-Pease mode, using the PNNL composition for T91, with displacement energies of 40 eV for Fe, Cr, Ni, V and Mn, 60 eV for Nb and Mo, 90 eV for W and 25 eV for all other elements [21]. T91 was irradiated to 17, 50 and 150 dpa with helium-to-dpa ratios of 0, 0.02, 0.2 and 4 appm He/dpa while HT9 was irradiated to 188 dpa with helium-to-dpa ratios of 0, 0.06 and 4 appm He/dpa. The helium-to-dpa ratio was non-uniform for the HT9 irradiations. However, this was not expected to significantly influence the results in the area of interest at 500–700 nm from the sample surface. The damage and helium implantation profiles are shown in Figure 1.

Each irradiation used J-type thermocouples welded to the sample surface to calibrate a 2D FLIR® Thermal Imaging System so that the temperature could be monitored in multiple locations on the sample during irradiation. Temperature control was maintained within a 2-sigma value of better than ±8°C by using an electronic cartridge heater and air cooling through the back of the irradiation stage. The irradiations were performed at 445°C for T91 and 460°C for HT9.

The pressure in the vacuum chamber was maintained below 10^{-7} torr ($<1.3 \times 10^{-5}$ Pa). To prevent any possible carbon contamination during irradiation, the stage containing the sample and the vacuum chamber were plasma cleaned using an Evactron EP Series Plasma De-Contaminator with a forward power of 15 W for 2 h prior to irradiation but after the samples and stage had been loaded. In addition, to prevent contamination during irradiation, a cold trap cooled by liquid nitrogen encircled the stage [27]. Additional information on the instrumentation and methodology used for dual-ion irradiations performed in MIBL can be found in [26].

2.3. Post-irradiation characterization

Transmission electron microscopy (TEM) specimens were prepared after irradiation at the Michigan Center for Materials Characterization (MC²) on either a Thermo Fisher Helios Nanolab 650 or a Thermo Fisher Nova 200 Nanolab focused ion beam (FIB) system. At least two liftouts were produced and analyzed for each irradiation condition. The same liftout procedure used for the previous studies of the T91 was also used here [21,22]. Two additional steps

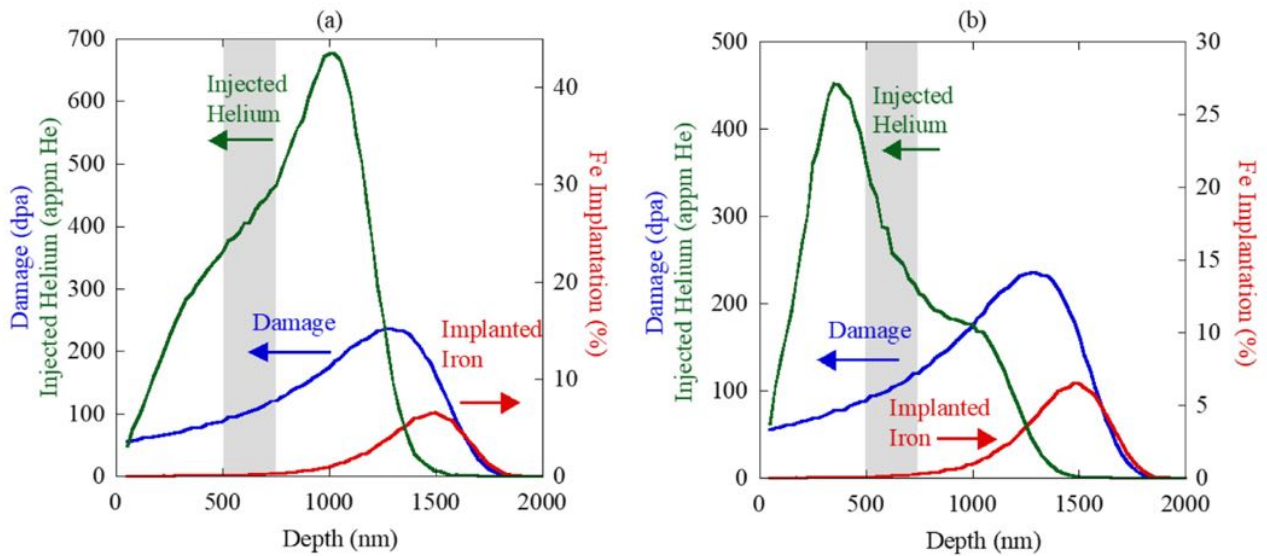


Figure 1. Damage profile (blue), injected helium profile (green) and implanted iron profile (red) for dual ion irradiated to 100 dpa with 4 appm He/dpa in (a) T91 at 445°C and (b) HT9 at 460°C. The shaded box shows the depth range from which the microstructural data was collected for this work.

were added to the typical FIB liftout process. First, the lamella was thinned in sections to produce two thick window frames to prevent bending as the thickness approached electron transparent thickness. Second, a two-step low energy (5 keV and 2 keV) polish was used to perform the final thinning from ~150 nm to 80–100 nm to effectively eliminate any visible FIB damage.

Imaging for the TEM specimens for this study was performed on multiple microscopes using different techniques to accurately quantify the microstructure. Cavities were characterized using high-angle annular dark field (HAADF) scanning transmission electron microscopy (STEM) on a either JEOL 2100F or a Thermo Fisher Tecnai G2 F30 at MC². Additional characterization of cavities smaller than 2 nm in diameter was performed on a Thermo Fisher Talos F200X and a JEOL 21010F at MC² using over and underfocused bright field (BF) transmission electron microscopy (TEM) imaging with a Gatan CCD camera with 4k resolution. Finally, dislocations were imaged in STEM BF using a JEOL 2100F and a Thermo Fisher Talos F200X near the [001] or [011] zone axis using a similar methodology as Yao et al. [28] and Parish et al. [29] to simultaneously image and distinguish between $a\langle 100 \rangle$ loops, $a/2\langle 111 \rangle$ loops and dislocation lines. Finally, the thickness of the liftouts was measured using electron energy loss spectroscopy (EELS). While the entire depth of irradiation was imaged, due to the shallow depth of penetration of 5 MeV Fe⁺⁺, a depth interval 300–900 nm from the surface was selected for data collection to avoid effects both from injected interstitials and the free surface [5,17]. To limit the variation in damage across the examined region, the window of analysis for this work was further reduced to 500–700 nm.

After collection of the images, features were hand-counted using ImageJ software to measure the diameter and estimate the density. HAADF STEM images were used to quantify cavities greater than 2 nm in diameter within depth bins of 100 nm. BF TEM images were used to estimate the diameter and density of cavities with diameters less than 2 nm in diameter using an objective aperture of 20 μ m. Finally, BF STEM images were used to quantify the diameter and density of dislocation loops after irradiation.

The swelling in the material was estimated using the measured cavity diameters. The volume of each cavity was calculated assuming a spherical shape. The sum of the volume of each cavity within a bin was effectively the change in volume, ΔV , for the bin. Swelling was then calculated as the change in volume divided by the original volume, yielding the swelling for any specific depth

bin, in %, as:

$$\text{Swelling (\%)} = \frac{\frac{\pi}{6} \sum_{i=1}^N d_i^3}{l \times w \times \delta - \frac{\pi}{6} \sum_{i=1}^N d_i^3} \times 100, \quad (1)$$

where N is the number of cavities in the bin, d_i is the diameter of the i th cavity, l is the length of area examined, w is the width of the bin and δ is the thickness of the TEM liftout.

Sink strengths for each of the features were also calculated. The cavity sink strengths were calculated assuming spherical cavities from the size distribution as $\sum_{i=1}^N 4\pi r_i \rho_i$, where N is the number of bins in the size distribution, r_i is the average cavity radius in the bin and ρ_i is the density of cavities within the bin. The dislocation network density was calculated using the methodology established by Smith et al. [30], counting the number of intersections of dislocation lines with an equidistant circular gird. The dislocation loops were converted into a line length by calculating their circumference and then multiplying by their density: $2\pi r \rho_d$, where r is the average loop radius and ρ_d is the loop density. The addition of the loop and network sink strengths determines the total dislocation sink strength.

3. Results

The results are organized by the alloy and then by microstructural feature. Cavities were observed under all irradiation conditions, typically with a bimodal distribution. While a spectrum of cavity sizes was present, the bimodal peaks are important feature in which the first peak consists of cavities that dominate the sink strength in the bias-driven growth regime, while the larger cavities in the second peak drive increased swelling in the bias-driven growth regime. To provide a framework for presenting and discussing the results, cavities, bubbles and voids must be defined. Cavities are the agglomeration of vacancies or vacancies and helium to a size visible in TEM and refers to both bubbles and voids. A bubble was defined to be any feature that falls in the first peak of the bimodal cavity size distribution, and a void was defined to be any feature that lies in the second peak of the bimodal cavity size distribution. If only one peak was present in the cavity size distribution (as was the case without helium), all features were classified as voids.

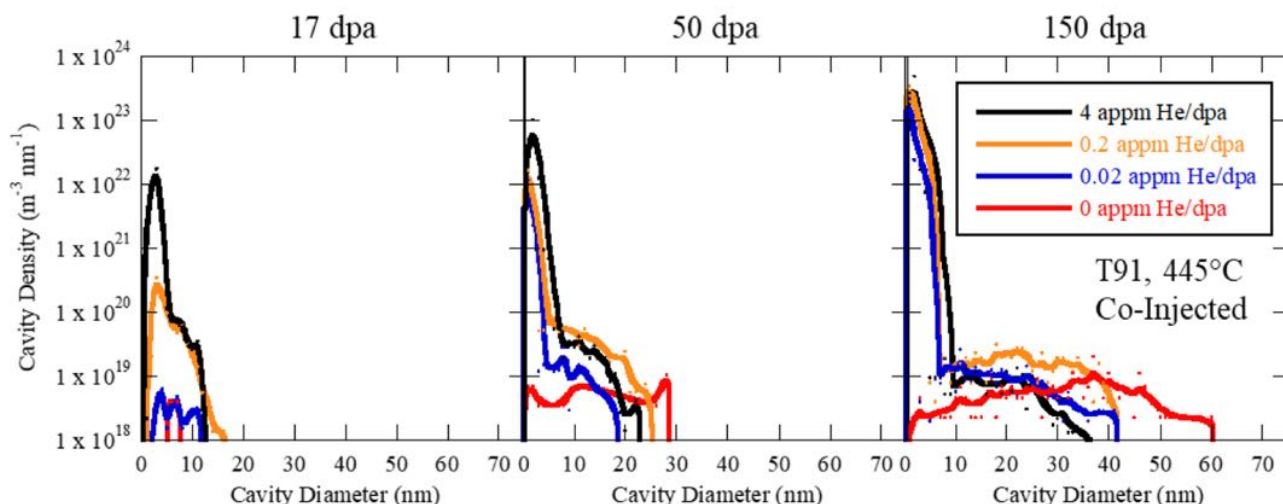


Figure 2. Cavity size distributions for dual-ion irradiated T91 at 445°C with 0 (red), 0.02 (blue), 0.2 (orange) and 4 (black) appm He/dpa at 17, 50 and 150 dpa. (For interpretation of the references to color in this figure legend, the reader is referred to the web version of this article.)

3.1. T91

The cavity size distributions are plotted for each damage level in Figure 2. Bimodal size distributions are observed for all conditions in which helium was injected for all damage levels. While the argument could be made that some of the conditions, particularly the 0.02 appm He/dpa case at 17 dpa, are not bimodal, it is likely due to either the limited number of cavities counted under the specific condition or normal size variation. In addition, consistent with the observed increase in average void diameter, the width of the size distribution increases with increasing damage level.

The evolution of the void microstructure as a function of helium co-injection rate for each of the damage levels for all irradiation conditions (17, 50 and 150 dpa) are shown in Figure 3. The average void diameter is relatively constant with helium co-injection rates of 17 and 50 dpa, with the largest average diameter of 6.9 ± 1 nm at 0 appm He/dpa to the smallest average diameter of 5.8 ± 1 nm at 0.02 appm He/dpa at 17 dpa. At 50 dpa, the largest average diameter was 11 ± 1 nm without helium, dropped to 8.1 ± 1 nm with 0.02 appm He/dpa and 9.9 ± 1 nm with 0.2 appm He/dpa, and ended with the lowest average diameter of 8.0 ± 1 nm with 4 appm He/dpa. At the highest damage level, the average void diameter drops significantly between 0 and 4 appm He/dpa. As shown in Figure 3(b), the void density for the first two damage levels of 17 and 50 dpa increases with increasing helium co-injection rate, but at 150 dpa, the trend changes slightly as the density at the highest helium co-injection rate of 4 appm He/dpa decreases. The resulting swelling maximum occurs at the highest helium co-injection rates at 17 dpa, shifting to an intermediate helium co-injection rates at 50 dpa, and finally peaks at zero helium at 150 dpa.

The bubble evolution with damage level for each helium co-injection rate is plotted in Figure 4. Only one peak was observed in the size distribution without the implantation of helium indicating that not bubbles formed, as expected. The bubble diameter varies little with appm He/dpa, Figure 4a, but varies with damage level, from ~ 3 nm at 17 dpa to ~ 2 nm at 50 dpa and ~ 1 nm at 150 dpa. The bubble density in Figure 4(b) shows a monotonic increase in density with increasing damage level. The increase was more pronounced at the lower damage levels. Of particular interest is the change in the relative bubble density. At 17 dpa, the bubble density increases monotonically with increasing helium co-injection rate. As the damage level is increased to 50 dpa, the bubble density at both 0.02 and 0.2 appm He/dpa increase by almost two orders of

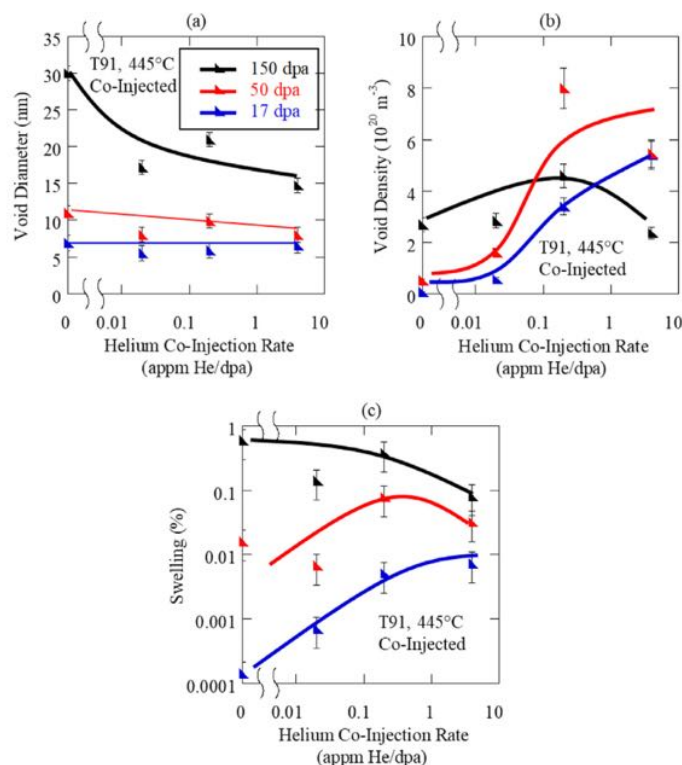


Figure 3. Average void diameter (a), void density (b) and swelling (c) as a function of helium co-injection rate (appm He/dpa) for dual-ion irradiated T91 at 445°C at 17 (blue), 50 (red) and 150 (black) dpa. (For interpretation of the references to color in this figure legend, the reader is referred to the web version of this article.)

magnitude while the density at 4 appm He/dpa only increases by about an order of magnitude. The change is not as significant as the damage level increases to 150 dpa, but the bubble density at 0.02 and 0.2 appm He/dpa still increases by a larger amount than the bubble density at 4 appm He/dpa.

Dislocations loops were observed to form under all irradiation conditions in T91. STEM-BF images of dislocation loops were collected for each helium co-injection rate irradiated at 445°C to 17 dpa and for all damage levels at 0.2 appm He/dpa. The average dislocation loop diameters and number densities are tabulated in Table 3 and plotted in Figure 5. The primary dislocation loops ob-

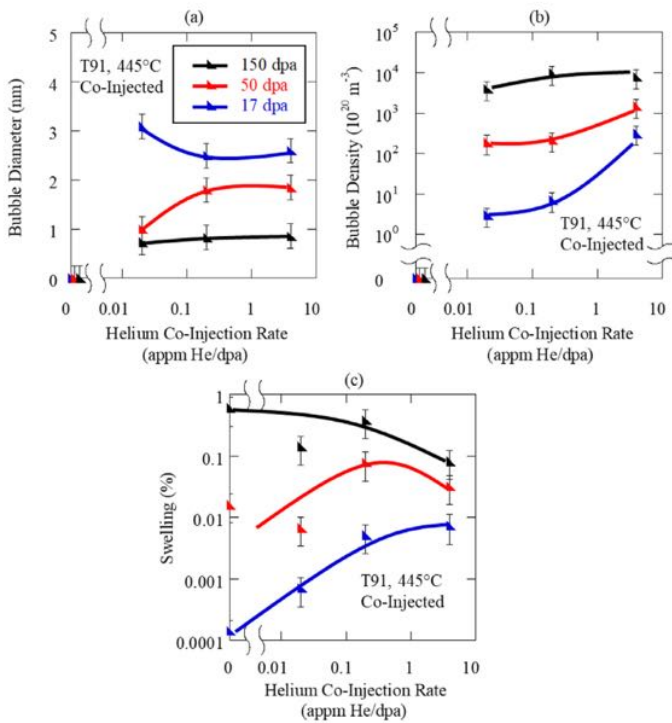


Figure 4. Average bubble diameter (a), bubble density (b) and swelling (c) for dual-ion irradiated T91 at 445°C to 17 (blue), 50 (red) and 150 (black) dpa. (For interpretation of the references to color in this figure legend, the reader is referred to the web version of this article.)

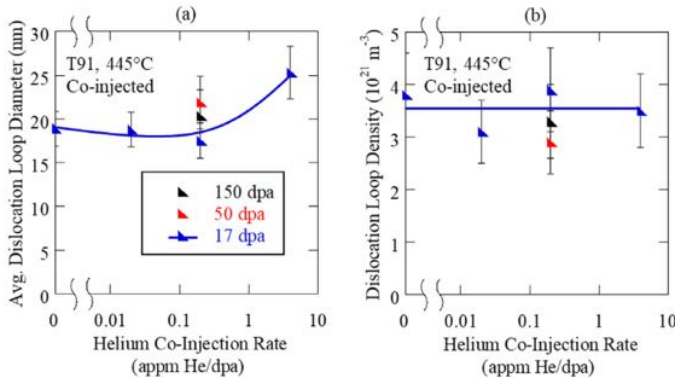


Figure 5. Average dislocation loop diameter (a) and dislocation loop density (b) for dual-ion irradiated T91 at 445°C to 17 (blue) and 0, 0.02, 0.2 and 4 appm He/dpa and at 0.2 appm He/dpa at 17 (blue), 50 (red) and 150 (black) dpa. A line has been added to the 17 dpa data to guide the eyes. (For interpretation of the references to color in this figure legend, the reader is referred to the web version of this article.)

served at each helium co-injection rate were $a\langle 100 \rangle$ dislocation loops with very few $a/2\langle 111 \rangle$ dislocation loops observed. The average dislocation loop diameter did not change significantly with helium co-injection rate at 17 dpa from 18 ± 3 nm to 25 ± 3 nm or with damage level at 0.2 appm He/dpa from 18 ± 3 nm to 22 ± 3 nm. The dislocation loop density did not significantly change with helium co-injection rate at 17 dpa in the range of $3.1 \pm 0.5 \times 10^{21} \text{ m}^{-3}$ to $3.9 \pm 0.5 \times 10^{21} \text{ m}^{-3}$ or with damage level at 0.2 appm He/dpa in the range of $2.9 \pm 0.5 \times 10^{21} \text{ m}^{-3}$ to $3.9 \pm 0.5 \times 10^{21} \text{ m}^{-3}$. Because the dislocation loop microstructure was not observed to change significantly with damage level at 0.2 appm He/dpa, it was not measured at any other helium level. Dislocation lines were observed at all helium co-injection rates and no significant alteration of the existing network dislocation density was noted compared to the as-tempered condition.

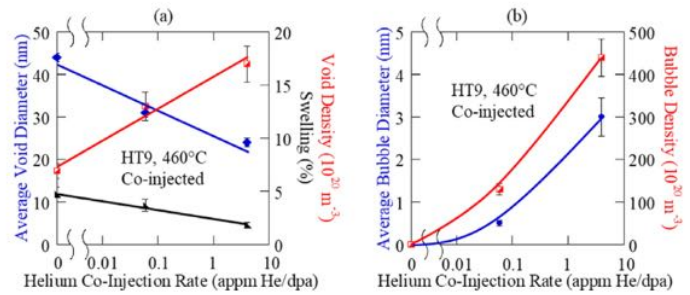


Figure 6. Void and swelling behavior (a) and bubble behavior (b) as a function of helium co-injection rate in HT9 dual-ion irradiated at 460°C to 188 dpa. Average diameter is shown in blue, density is shown in red and swelling is shown in black. (For interpretation of the references to color in this figure legend, the reader is referred to the web version of this article.)

3.2. HT9

Voids were observed to form under all helium injection rates in HT9 at 188 dpa and 460°C while bubbles were only observed for the two helium injection rates: 0.06 appm He/dpa and 4 appm He/dpa. The void behavior is plotted in Figure 6(a) and tabulated in Table 2. The average void diameter was highest at 0 appm He/dpa with a value of 44 ± 1 nm and dropped monotonically with helium co-injection rate. Void density exhibited the opposite trend with helium co-injection rate with a value of $6.9 \times 10^{20} \text{ m}^{-3}$ at 0 appm He/dpa and a maximum of $17 \times 10^{20} \text{ m}^{-3}$ at 4 appm He/dpa. Swelling followed a similar trend to void diameter with a maximum of 4.7% with 0 appm He/dpa, decreasing to 3.7% at 0.06 appm He/dpa and reaching a minimum of 1.8% at 4 appm He/dpa. As shown in Table 2, even with the differences in void evolution, the void sink strength was relatively constant, only varying between $1.9\text{--}2.6 \times 10^{14} \text{ m}^{-2}$.

The behavior for bubbles is plotted in Figure 6(b) and tabulated in Table 2. No bubbles were observed without the injection of helium. With increasing helium co-injection rate, both the average bubble diameter and the bubble density increased from 0.5 nm and $130 \times 10^{20} \text{ m}^{-3}$ at 0.06 appm He/dpa to 3 nm and $440 \times 10^{20} \text{ m}^{-3}$ at 4 appm He/dpa. In contrast to the void sink strength, these differences in bubble evolution significantly changed the bubble sink strength, reaching a value of $8.3 \times 10^{14} \text{ m}^{-2}$ at 4 appm He/dpa.

The cavity size distribution for the three He injection rates at 188 dpa are plotted in Figure 7. Without the addition of helium, a unimodal distribution develops as expected. With the addition of a small amount of helium (0.06 appm He/dpa), a narrow lower peak develops producing a bimodal distribution. With the addition of helium at higher rates (4 appm He/dpa), the peak both increases in height and broadens in width. The trends for the second peak of the distribution (or the single mode of the 0 appm He/dpa condition) follow a slightly different trend. With the addition of helium, the second mode shrinks in width, spanning a range of ~ 60 nm without any helium, but only ~ 40 nm at the highest helium injection rate. Conversely, the height of the distribution increases with increasing helium co-injection rate.

Dislocations loops were observed to form under all irradiation conditions in HT9. STEM-BF images of dislocation loops were collected for each irradiation condition. A summary of the average dislocation loop diameters and number densities are tabulated in Table 3 and plotted in Figure 8. The primary dislocation loops observed at each helium co-injection rate were $a\langle 100 \rangle$ dislocation loops with very few $a/2\langle 111 \rangle$ dislocation loops observed. The average dislocation loop diameter did not change significantly with helium co-injection rate at 188 dpa and the dislocation loop density decreased slightly with helium co-injection rate at 188 dpa in

Table 2

Summary of void and bubble microstructure after ion irradiation.

Material/ Temp (°C)	Damage Level (dpa)	Helium-to-dpa Ratio (appm He/dpa)	Average Void Diameter (nm)	Void Density (10 ²⁰ m ⁻³)	Average Bubble Diameter (nm)	Bubble Density (10 ²⁰ m ⁻³)	Bubble Sink Strength (10 ¹⁴ m ⁻²)	Cavity Sink Strength (10 ¹⁴ m ⁻²)	Swelling (%)
T91/445	17	0.00	6.9 ± 1	0.082 ± 0.008	N.O.	N.O.	N.O.	0.004 ± 0.0008	0.00014 ± 0.00002
		0.02	5.8 ± 1	1.1 ± 0.1	3.1 ± 1	3.0 ± 0.3	0.058 ± 0.01	0.12 ± 0.024	0.0044 ± 0.0007
		0.20	5.9 ± 1	3.4 ± 0.3	2.5 ± 1	7.0 ± 0.7	0.11 ± 0.02	0.24 ± 0.048	0.0051 ± 0.0008
		4.00	6.6 ± 1	4.9 ± 0.5	2.6 ± 1	320 ± 30	5.2 ± 1	5.4 ± 1	0.0073 ± 0.001
	50	0.00	11 ± 1	0.53 ± 0.05	N.O.	N.O.	N.O.	0.037 ± 0.007	0.016 ± 0.002
		0.02	8.1 ± 1	1.6 ± 0.2	1.6 ± 1	190 ± 20	1.9 ± 0.4	2.0 ± 0.4	0.00675 ± 0.001
		0.20	9.9 ± 1	8.0 ± 0.8	1.8 ± 1	220 ± 20	2.5 ± 0.5	3.0 ± 0.6	0.078 ± 0.01
		4.00	8.0 ± 1	5.5 ± 0.6	1.9 ± 1	1500 ± 150	17 ± 3	18 ± 3	0.032 ± 0.005
	150	0.00	30 ± 1	2.7 ± 0.3	N.O.	N.O.	N.O.	0.51 ± 0.1	0.6 ± 0.09
		0.02	17 ± 1	3.3 ± 0.3	0.73 ± 1	4000 ± 400	18 ± 4	19 ± 4	0.14 ± 0.02
		0.20	21 ± 1	2.9 ± 0.3	0.83 ± 1	9600 ± 1000	50 ± 10	51 ± 10	0.38 ± 0.06
		4.00	15 ± 1	2.4 ± 0.2	1.2 ± 1	7900 ± 800	60 ± 10	60 ± 10	0.082 ± 0.01
HT9/460	188	0.00	44 ± 1	6.9 ± 0.7	N.O.	N.O.	N.O.	1.9 ± 0.4	4.7 ± 0.7
		0.06	31 ± 1	13 ± 1	0.50 ± 1	130 ± 10	0.39 ± 0.08	2.8 ± 0.6	3.7 ± 0.6
		4.00	24 ± 1	17 ± 2	3.0 ± 1	440 ± 40	8.3 ± 2	11 ± 2	1.8 ± 0.3

Table 3

Summary of dislocation microstructure after dual ion irradiation.

Material/Temp (°C)	Damage Level (dpa)	Helium Co-Injection Rate (appm /dpa)	Number of Dislocation Loops Examined	Dislocation Loop Density (10 ²¹ m ⁻³)	Average Dislocation Loop Diameter (nm)	Dislocation Loop Line Density (10 ¹³ m ⁻²)	Total Dislocation Loop Sink Strength (10 ¹⁴ m ⁻²)
T91/445	17	0	156	3.8 ± 0.8	19 ± 2	2.3 ± 0.5	2.8 ± 0.6
	17	0.02	141	3.1 ± 0.6	19 ± 2	1.8 ± 0.4	2.3 ± 0.5
	17	0.22	104	3.9 ± 0.8	18 ± 2	2.1 ± 0.5	2.7 ± 0.6
	50	0.22	113	2.9 ± 0.6	22 ± 3	2.1 ± 0.5	2.6 ± 0.6
	150	0.22	107	3.3 ± 0.7	20 ± 3	2.0 ± 0.5	2.6 ± 0.6
	17	4.3	103	3.5 ± 0.7	25 ± 3	2.8 ± 0.6	2.5 ± 0.6
HT9/460	0	188	31	1.6 ± 0.3	34 ± 4	1.7 ± 0.4	2.2 ± 0.5
	0.06	188	47	0.31 ± 0.06	37 ± 5	0.36 ± 0.09	0.46 ± 0.1
	4	188	29	0.73 ± 0.15	35 ± 5	0.80 ± 0.20	1.0 ± 0.2

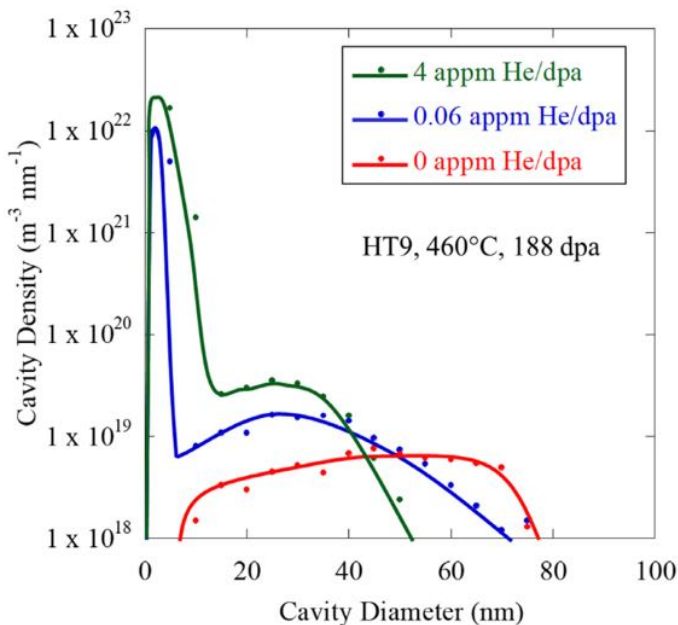


Figure 7. Cavity size distributions for dual-ion irradiated HT9 at 460°C and 188 dpa with 0 (red), 0.06 (blue) and 4 (green) appm He/dpa. (For interpretation of the references to color in this figure legend, the reader is referred to the web version of this article.)

the range of $0.31 \pm 0.1 \times 10^{21} \text{ m}^{-3}$ to $1.6 \pm 0.5 \times 10^{21} \text{ m}^{-3}$ but was likely due to local variation and the relatively limited number of counted loops. Dislocation lines were observed at all helium co-injection rates and no significant alteration of the existing net-

work dislocation density was noted compared to the as-tempered condition.

4. Discussion

Cavity evolution in both alloys depends on both the rate at which helium is co-injected into the samples as well as the total damage level. At the lowest damage level examined, 17 dpa, swelling was maximized at the highest helium co-injection rate. The presence of co-injected helium served to create nucleation sites such that a high density of void was established early (low damage level). As seen in Figure 3(b), the void density for both the 0 appm He/dpa and the 0.02 appm He/dpa conditions increased as the damage level was raised from 17 to 50 dpa indicating that both irradiation conditions were still in the nucleation-dominated regime at 17 dpa. This observation is consistent with previous work performed by Getto [31] and Toloczko [16,17] that showed that the nucleation regime extends out to at least tens of dpa.

As the damage level is increased, swelling transitioned (the so-called transition regime) from a nucleation-dominated regime in which void density drives the increase in swelling, to a growth-dominated regime in which void growth drives the increase in swelling. Thus, it would be expected that the effect of helium on swelling would change as well. Recall that the He/dpa value at which swelling was a maximum shifted from 4 appm He/dpa at 17 dpa to 0.2 appm He/dpa at 50 dpa to 0 appm He/dpa at 150 dpa, indicating that there is indeed a change in the process. To determine how swelling depends on He content, the swelling regime of each helium co-injection condition examined using the simple cavity growth rate equation [32]:

$$\frac{dr}{dt} = \frac{\Omega}{r} \left[D_v C_v - D_i C_i - D_v C_v \exp\left(\frac{2\gamma}{r} - p_g\right) \right], \quad (2)$$

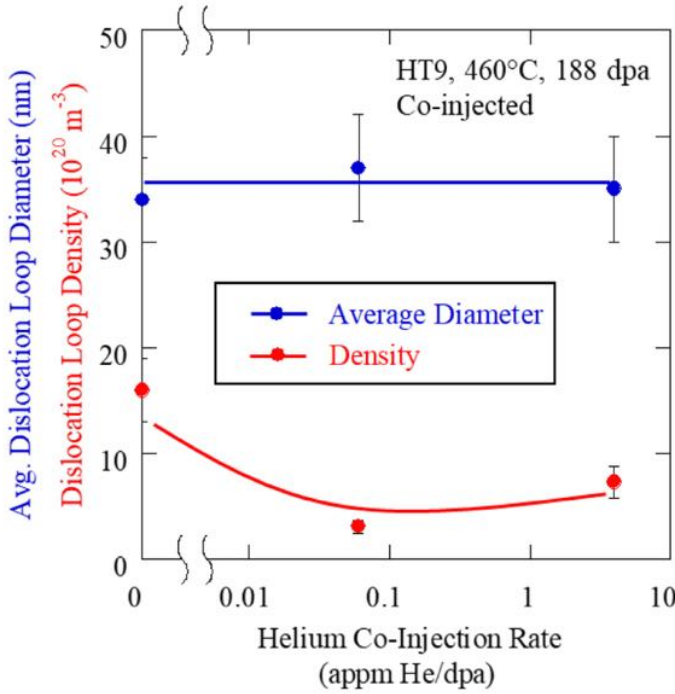


Figure 8. Average dislocation loop diameter (blue) and dislocation loop density (red) for dual-ion irradiated HT9 at 460°C to 188 dpa. (For interpretation of the references to color in this figure legend, the reader is referred to the web version of this article.)

Table 4

Table of input parameters for alloy T91 used in the cavity growth rate equation.

Parameter	Value	Reference
Temperature, T	Input parameter	This work
Damage Rate, K_0	Input parameter	This work
Helium Co-Injection Rate	Input parameter	This work
N	8.34×10^{22} at/cm ³	[33]
Lattice parameter (a)	0.288 nm	[18,33]
Sink strength	From microstructure	This work and [22]
ω_i	2.9×10^{12} s ⁻¹	[33]
ω_v	1.6×10^{13} s ⁻¹	[33]
γ	1.75 J/m ²	[18]
E_{vm}	0.63 eV	[18]
E_{vf}	1.6 eV	[33]
E_{im}	0.35 eV	[33]
S_f	2.17k	[32]
Dislocation Bias	5%	

where $D_v C_v$ represents the arrival of vacancies, $D_i C_i$ represents the arrival of interstitial atoms and $D_v C_v \exp(\frac{2\gamma}{r} - p_g)$ represents the thermal emission of vacancies. Furthermore, r is the radius of a cavity, t is time (and can be converted to dpa using the damage rate), Ω is the atomic volume of the alloy, D_x is the diffusion rate for vacancies (v) or interstitials (i), C_x is the concentration of vacancies (v) or interstitials (i), $C_{v,T}$ is the thermal concentration of vacancies, γ is the surface energy of the alloy and p_g is the gas pressure. Since the growth of the larger cavities, which are not gas stabilized, drive swelling in the growth dominated regime, the gas pressure is assumed to be negligible and has been treated as 0 for all subsequent calculations. The point defect concentrations are calculated using the steady-state point defect equations:

$$0 = K_0 - K_{iv} C_i (C_v + C_{v,T}) - k_{(i,v)}^2 D_{(i,v)} C_{(i,v)}, \quad (3)$$

where K_0 is the damage rate, K_{iv} is the recombination coefficient and k_x^2 is the sink strength for vacancies (v) or interstitials (i). The inputs for these equations are provided in Table 4. The sink

strengths for dislocations and cavities, respectively, are calculated from the size distributions using:

$$k_{dis}^2 = \sum_j 2\pi r_j \rho_j, \quad (4)$$

and

$$k_{cav}^2 = \sum_j 4\pi r_j \rho_j, \quad (5)$$

where r_j is the average radius of and ρ_j is the defect density in bin j .

The only place in which helium appears directly in the simple cavity growth rate equation is in the gas pressure term. However, it is reasonable to assume that for voids (particularly large ones), the helium pressure is small and can be neglected, so helium must be influencing the cavity growth in some other way.

Helium can indirectly influence the cavity growth rate equation by stabilizing a bubble microstructure and increasing the overall sink strength in the system, reducing the vacancy supersaturation, and thus, the flux of vacancies to voids. Using Eqs. 4 and 5, the cavity and bubble sink strengths at 50 and 150 dpa, the dislocation sink strengths and swelling are plotted as a function of He/dpa for T91 at 445°C in Figure 9a and tabulated in Table 2. Recall that dislocations were only measured at a single helium-to-dpa ratio and did not show a significant difference with damage level as shown in Table 3. As such, only the 17 dpa dislocation sink strength was plotted. As shown in Figure 9a, swelling follows the difference between the dislocation and cavity (voids + bubbles) sink strengths. Swelling is maximized with 0.2 appm He/dpa at 50 dpa in T91 when the cavity sink strength is just below the dislocations sink strength. As the damage level increased to 150 dpa, the intersection of dislocation and cavity sink strengths occurs at very low He/dpa level so swelling decreases from that value onward. It is important to note that the bubble sink strength is the main component of the cavity sink strength for all conditions in which bubbles were observed, suggesting that the helium stabilized bubbles are driving the increased sink strength in the microstructure. A similar analysis can be performed for the HT9 samples irradiated to 188 dpa at 460°C and shown in Figure 9b. At this damage level, swelling is inversely proportional to both the cavity sink strength and the helium-to-dpa ratio with the maximum swelling observed at zero helium and dropping off monotonically as the helium injection rate increases.

To determine whether these differences in sink strength could have driven the observed shift in maximum swelling from high to low helium co-injection rate with increasing damage level, the swelling rate, dS/dt was calculated using the cavity size distributions, the calculated sink strengths, and the parameters in Table 4. Since swelling can be calculated from the total volume of all cavities, a simple time derivative can estimate the swelling rate from the rate of change of the cavity volumes according to:

$$\frac{dS}{dt} = 4\pi r^2 \rho \frac{dr}{dt} = \sum_j 4\pi r_j^2 \rho_j \frac{dr_j}{dt}, \quad (6)$$

where r_j was the average cavity radius in bin j , ρ_j was the cavity density in bin j , and $\frac{dr_j}{dt}$ was the growth rate calculate for a cavity in bin j using Eq. 2. The resulting swelling rate is plotted in Figure 10 along with the swelling rate calculated from the measured swelling values. First, it should be noted that the calculated and measured swelling rates are in reasonable agreement indicating that even though it is simple, the model captures most of the observed behavior. Second, the swelling rates line up very well with the shift in swelling observed in the data. Specifically, at 50 dpa, the maximum swelling rate occurs at 0.2 appm He/dpa, and then by 150 dpa, the maximum swelling shifts to zero He.

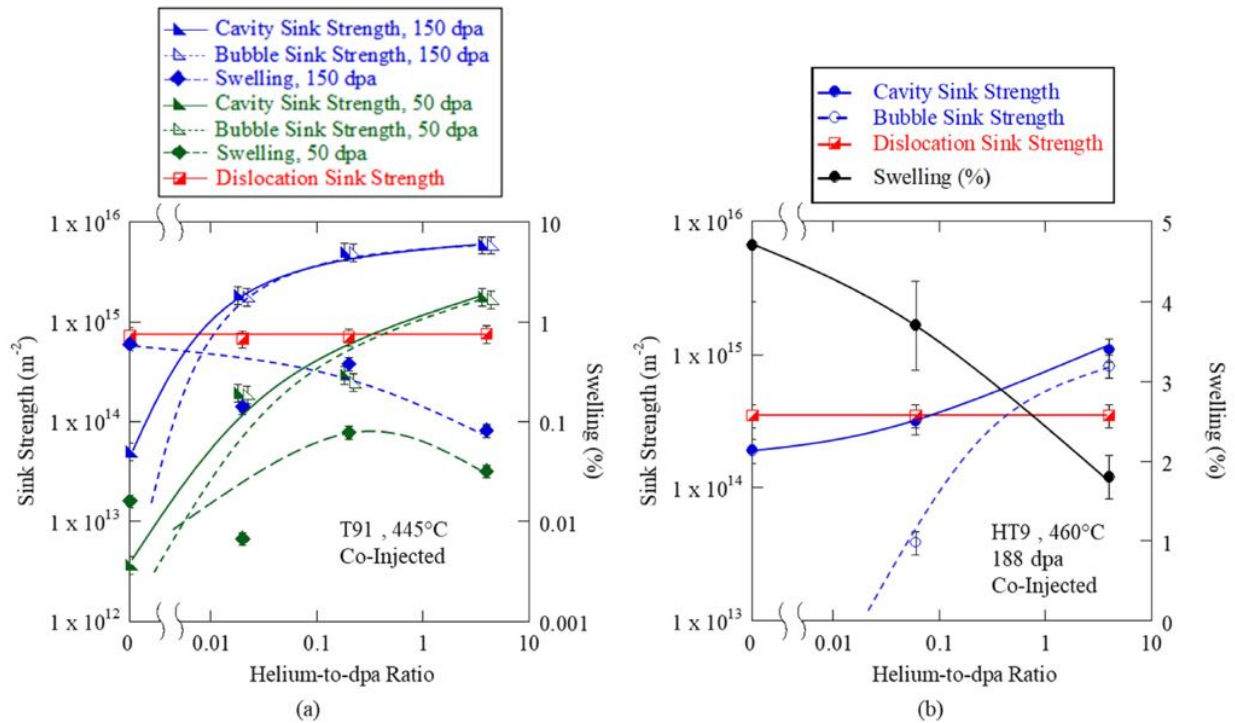


Figure 9. Sink strength and cavity trends with helium-to-dpa ratio in (a) T91 irradiated at 445°C to 50 dpa (triangles) and 150 dpa (diamonds) and (b) HT9 irradiated at 460°C to 188 dpa. Cavity sink strengths are shown in blue with solid markers and solid lines. Bubble sink strengths are shown in blue with open markers and dashed lines. Total dislocation sink strengths (loop and network) are shown in red squares with solid lines. And Swelling is shown in black with solid markers and solid lines. (For interpretation of the references to color in this figure legend, the reader is referred to the web version of this article.)

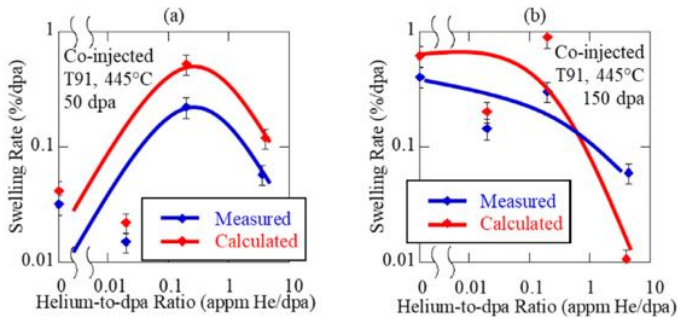


Figure 10. Measured (blue) and calculated (red) swelling rates as a function of helium-to-dpa ratio for dual-ion irradiated T91 at 445°C to 50 dpa (a) and 150 dpa (b). (For interpretation of the references to color in this figure legend, the reader is referred to the web version of this article.)

The behavior of swelling with helium is compared to work by others on similar alloys but with pre-injected He to separate out the effect of helium injection mode. Monterrosa et al. [12] used a different heat of T91 (C2269) that was pre-implanted with helium to levels of 0, 1, 10, 100 and 1000 appm He and then irradiated to 50, 150 and 300 dpa at 460°C. Under these conditions, the maximum swelling was observed to occur at an intermediate helium concentration of 10 appm He at 50 dpa which was the result of decreasing cavity size and increasing cavity density with He, producing the maximum swelling at an intermediate value of He. As the damage level increased to 150 dpa, the cavity density did not change for any helium concentration other than 0 appm He, indicating that helium had accelerated the nucleation of cavities. In contrast, the average diameter decreased monotonically with He, resulting in the highest cavity growth rate and swelling rate were observed with 0 appm He, which corresponded to the lowest sink

strength. Finally, as the damage level was increased to 300 dpa, the cavity density was observed to have saturated for all helium concentrations meaning that any changes in swelling were due solely from changes in cavity diameter. Cavity size decreased with He, resulting in the maximum swelling occurring at 0 appm H. Thus, the trend observed by Monterrosa was consistent with that in this study. This agreement suggests that the dependence of swelling on He content depends on dpa, but not on the helium injection method.

The work by Yamamoto et al. [19] mentioned previously, is revisited to establish the universality of these trends. They irradiated alloy F82H with 6.4 MeV Fe^{3+} ions and energy degraded He^+ ions. The data for different helium-to-dpa ratios were taken by looking at different depths within the sample. Two different nominal damage levels were produced: 10 dpa and 26 dpa. The maximum swelling was observed at 40 appm He/dpa at both nominal damage levels with the swelling dropping off as the helium-to-dpa dropped both at shallower and deeper depths. The number density did not change significantly with helium co-injection rate, so the difference in swelling was driven by differences in the cavity diameter. It is difficult to draw conclusions from these two data points in isolation since they are at relatively low damage level. However, taken with the previous discussion, it provides support for the idea that helium reduces swelling as the damage level increases.

This work combined with the work from Monterrosa et al. [12] and Yamamoto et al. [19] are plotted in Figure 11 and shows that across three different alloys (one with two different heats), and for both helium co-injection and pre-injection, the condition for maximum swelling is high helium concentrations at low damage levels shifting to low (or zero) helium concentration at higher damage levels. This behavior is driven by a reduction in the swelling rate due to an increase in the cavity sink strength caused by a helium-stabilized bubble microstructure.

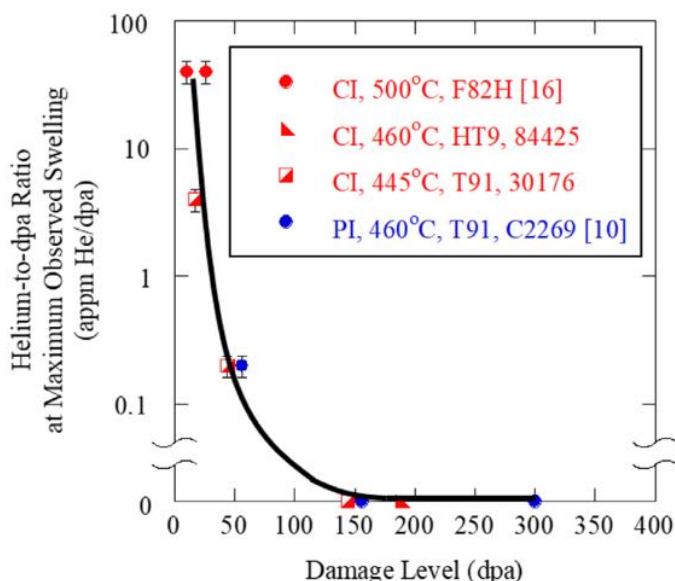


Figure 11. Helium-to-dpa Ratio at which the maximum swelling was observed in multiple ferritic-martensitic alloys and irradiation conditions under both pre-injection (PI) and co-injection (CI) [12,19].

5. Conclusions

Conclusions resulting from variation of both the damage level and the He injection rate and their effect on swelling are as follows:

- The helium-to-dpa ratio at which the maximum swelling occurs shifts to lower helium-to-dpa levels as the damage level increases in ferritic-martensitic steels
- The helium stabilized bubbles increase the cavity sink strength of the microstructure and reduce the growth rate of voids
- The trend holds for multiple heats and alloys of ferritic-martensitic steels
- The trend is irrespective of helium injection method; cold pre-injection or co-injection

Credit Authorship Contribution Statement

David Woodley: Conceptualization, Methodology, Software, Formal Analysis, Investigation, Data Curation, Writing – Original Draft, Visualization

Stephen Taller: Conceptualization, Methodology, Software, Formal analysis, Investigation, Writing – Review & Editing, Visualization

Zhijie Jiao: Conceptualization, Formal analysis, Investigation, Writing – Review & Editing, Visualization

Kai Sun: Investigation, Resources, Writing – Review & Editing

Gary S. Was: Conceptualization, Writing – Review & Editing, Supervision, Project administration, Funding acquisition

Declaration of Competing Interest

The authors declare that they have no known competing financial interests or personal relationships that could have appeared to influence the work reported in this paper.

Acknowledgements

Support for D. Woodley partially provided by a DOE NEUP Graduate Fellowship. Support for S. Taller partially from the DOE Office of Nuclear Energy's Nuclear Energy University Programs under contract DE-NE0000639. The authors gratefully acknowledge

O. Toader, F. Naab, T. Kubley and E. Uberseder at the Michigan Ion Beam Laboratory for their assistance with ion irradiations, the financial support of TerraPower, Inc. through research roundtable agreement DRDA 11-PAF05786, the University of Michigan College of Engineering, NSF Grants #DMR-0723032 for support of the JEOL 2100F Probe-Corrected AEM, #DMR-9871177 for support of the JEOL 2010F AEM and #DMR-0320740 for support of the Thermo Fisher Nova 200 Nanolab SEM/FIB, and technical support from the Michigan Center for Materials Characterization staff.

References

- [1] G.S. Was, D. Petti, S. Ukai, S. Zinkle, Materials for future nuclear energy systems, *J. Nucl. Mater.* 527 (2019) 151837, doi:10.1016/j.jnucmat.2019.151837.
- [2] S.J. Zinkle, G.S. Was, Materials challenges in nuclear energy, *Acta Mater* 61 (2013) 735–758, doi:10.1016/j.actamat.2012.11.004.
- [3] G.S. Was, Z. Jiao, E. Getto, K. Sun, A.M. Monterrosa, S.A. Maloy, O. Anderoglu, B.H. Sencer, M. Hackett, Emulation of reactor irradiation damage using ion beams, *Scr. Mater.* 88 (2014) 33–36, doi:10.1016/j.scriptamat.2014.06.003.
- [4] G.S. Was, J. Busby, T. Allen, E. Kenik, A. Jensson, S. Bruemmer, J. Gan, A. Edwards, P. Scott, Andreson, Emulation of neutron irradiation effects with protons: validation of principle, *J. Nucl. Mater.* 300 (2002) 198–216, doi:10.1016/S0022-3115(01)00751-6.
- [5] S.J. Zinkle, L.L. Snead, Opportunities and limitations for ion beams in radiation effects studies: Bridging critical gaps between charged particle and neutron irradiations, *Scr. Mater.* 143 (2018) 154–160, doi:10.1016/j.scriptamat.2017.06.041.
- [6] K. Farrell, Experimental effects of helium on cavity formation during irradiation—a review, *Radiat. Eff.* 53 (1980) 175–194, doi:10.1080/00337578008207114.
- [7] K. Farrell, P.J. Maziasz, E.H. Lee, L.K. Mansur, Modification of radiation damage microstructure by helium, *Radiat. Eff.* 78 (1983) 277–295, doi:10.1080/00337578308207378.
- [8] G.R. Odette, P.J. Maziasz, J.A. Spitznagel, Fission-fusion correlations for swelling and microstructure in stainless steels: Effect of the helium to displacement per atom ratio, *J. Nucl. Mater.* 104 (1981) 1289–1303, doi:10.1016/0022-3115(82)90779-6.
- [9] R.E. Stoller, The influence of helium on microstructural evolution: Implications for DT fusion reactors, *J. Nucl. Mater.* 174 (1990) 289–310, doi:10.1016/0022-3115(90)90242-F.
- [10] J.L. Brimhall, E.P. Simonen, Effect of helium on void formation in nickel, *J. Nucl. Mater.* 68 (1977) 235–243, doi:10.1016/0022-3115(77)90242-2.
- [11] K. Farrell, M.B. Lewis, N.H. Packan, Simultaneous bombardment with helium, hydrogen, and heavy ions to simulate microstructural damage from fission or fusion neutrons, *Scr. Metall.* 12 (1978) 1121–1124, doi:10.1016/0036-9748(78)90087-X.
- [12] A.M. Monterrosa, Z. Jiao, G.S. Was, The influence of helium on cavity evolution in ion-irradiated T91, *J. Nucl. Mater.* 509 (2018) 707–721, doi:10.1016/j.jnucmat.2018.06.033.
- [13] S. Taller, G.S. Was, Understanding bubble and void nucleation in dual ion irradiated T91 steel using single parameter experiments, *Acta Mater* 198 (2020) 47–60, doi:10.1016/j.actamat.2020.07.060.
- [14] F.A. Schmidt, P.R. Malmberg, J.A. Sprague, J.E. Westmoreland, Swelling Behavior of Commercial Ferritic Alloys, EM-12 and HT-9, as Assessed by Heavy Ion Bombardment, *Irradiat. Eff. Microstruct. Prop. Met.* (1976) 227.
- [15] J.J. Kai, G.L.L. Kulcinski, 14 MeV nickel-ion irradiated HT-9 ferritic steel with and without helium pre-implantation, *J. Nucl. Mater.* 175 (1990) 237–243, doi:10.1016/0022-3115(90)90212-6.
- [16] M.B. Toloczko, F.A. Garner, V.N. Voyevodin, V.V. Bryk, O.V. Borodin, V.V. Mel'nychenko, A.S. Kalchenko, Ion-induced swelling of ODS ferritic alloy MA957 tubing to 500 dpa, *J. Nucl. Mater.* 453 (2014) 323–333, doi:10.1016/j.jnucmat.2014.06.011.
- [17] E. Getto, Z. Jiao, A.M. Monterrosa, K. Sun, G.S. Was, Effect of pre-implanted helium on void swelling evolution in self-ion irradiated HT9, *J. Nucl. Mater.* 462 (2015) 458–469, doi:10.1016/j.jnucmat.2015.01.045.
- [18] E.M. Getto, The Co-Evolution of Microstructure Features in Self-Ion Irradiated HT9 at Very High Damage Levels, University of Michigan, 2016 <http://hdl.handle.net/2027.42/135912>.
- [19] T. Yamamoto, Y. Wu, G. Robert Odette, K. Yabuuchi, S. Kondo, A. Kimura, A dual ion irradiation study of helium-dpa interactions on cavity evolution in tempered martensitic steels and nanostructured ferritic alloys, *J. Nucl. Mater.* 449 (2014) 190–199, doi:10.1016/j.jnucmat.2014.01.040.
- [20] B.H. Sencer, J.R. Kennedy, J.I. Cole, S.A. Maloy, F.A. Garner, Microstructural stability of an HT-9 fuel assembly duct irradiated in FFTF, *J. Nucl. Mater.* 414 (2011) 237–242, doi:10.1016/j.jnucmat.2011.03.050.
- [21] Z. Jiao, S. Taller, K. Field, G. Yeli, M.P. Moody, G.S. Was, Microstructure evolution of T91 irradiated in the BOR60 fast reactor, *J. Nucl. Mater.* 504 (2018) 122–134, doi:10.1016/j.jnucmat.2018.03.024.
- [22] S. Taller, Z. Jiao, K. Field, G.S. Was, Emulation of fast reactor irradiated T91 using dual ion beam irradiation, *J. Nucl. Mater.* 527 (2019) 151831, doi:10.1016/j.jnucmat.2019.151831.

- [23] T.S. Byun, J.-H. Baek, O. Anderoglu, S.A. Maloy, M.B. Toloczko, Thermal annealing recovery of fracture toughness in HT9 steel after irradiation to high doses, *J. Nucl. Mater.* 449 (2014) 263–272, doi:[10.1016/j.jnucmat.2013.07.064](https://doi.org/10.1016/j.jnucmat.2013.07.064).
- [24] S.A. Maloy, M. Toloczko, J. Cole, T.S. Byun, Core materials development for the fuel cycle R&D program, *J. Nucl. Mater.* 415 (2011) 302–305, doi:[10.1016/j.jnucmat.2011.04.027](https://doi.org/10.1016/j.jnucmat.2011.04.027).
- [25] B.H. Sencer, J.R. Kennedy, J.I. Cole, S.a. Maloy, F.a. Garner, Microstructural analysis of an HT9 fuel assembly duct irradiated in FFTF to 155 dpa at 443 C, *J. Nucl. Mater.* 393 (2009) 235–241, doi:[10.1016/j.jnucmat.2009.06.010](https://doi.org/10.1016/j.jnucmat.2009.06.010).
- [26] S. Taller, D. Woodley, E. Getto, A.M. Monterrosa, Z. Jiao, O. Toader, F. Naab, T. Kubley, S. Dwaraknath, G.S. Was, Multiple ion beam irradiation for the study of radiation damage in materials, *Nucl. Instruments Methods Phys. Res. Sect. B Beam Interact. with Mater. Atoms.* 412 (2017) 1–10, doi:[10.1016/j.nimb.2017.08.035](https://doi.org/10.1016/j.nimb.2017.08.035).
- [27] G.S. Was, S. Taller, Z. Jiao, A.M. Monterrosa, D. Woodley, D. Jennings, T. Kubley, F. Naab, O. Toader, E. Uberseder, Resolution of the carbon contamination problem in ion irradiation experiments, *Nucl. Instruments Methods Phys. Res. Sect. B Beam Interact. with Mater. Atoms.* 412 (2017) 58–65, doi:[10.1016/j.nimb.2017.08.039](https://doi.org/10.1016/j.nimb.2017.08.039).
- [28] B. Yao, D.J. Edwards, R.J. Kurtz, TEM characterization of dislocation loops in irradiated bcc Fe-based steels, *J. Nucl. Mater.* 434 (2013) 402–410, doi:[10.1016/j.jnucmat.2012.12.002](https://doi.org/10.1016/j.jnucmat.2012.12.002).
- [29] C.M. Parish, K.G. Field, A.G. Certain, J.P. Wharry, Application of STEM characterization for investigating radiation effects in BCC Fe-based alloys, *J. Mater. Res.* 30 (2015) 1275–1289, doi:[10.1557/jmr.2015.32](https://doi.org/10.1557/jmr.2015.32).
- [30] C.S. Smith, L. Guttman, Measurement of Internal Boundaries in Three-Dimensional Structures By Random Sectioning, *JOM* 5 (1953) 81–87, doi:[10.1007/BF03397456](https://doi.org/10.1007/BF03397456).
- [31] E. Getto, K. Sun, A.M. Monterrosa, Z. Jiao, M.J. Hackett, G.S. Was, Void swelling and microstructure evolution at very high damage level in self-ion irradiated ferritic-martensitic steels, *J. Nucl. Mater.* 480 (2016) 159–176, doi:[10.1016/j.jnucmat.2016.08.015](https://doi.org/10.1016/j.jnucmat.2016.08.015).
- [32] G.S. WAS, *Fundamentals of Radiation Materials Science*, 2nd Ed, Springer, New York, New York, NY, 2017, doi:[10.1007/978-1-4939-3438-6](https://doi.org/10.1007/978-1-4939-3438-6).
- [33] J.P. Wharry, G.S. Was, The mechanism of radiation-induced segregation in ferritic-martensitic alloys, *Acta Mater* 65 (2014) 42–55, doi:[10.1016/j.actamat.2013.09.049](https://doi.org/10.1016/j.actamat.2013.09.049).